Desalination 593 (2025) 118201

Contents lists available at ScienceDirect

Desalination

journal homepage: www.elsevier.com/locate/desal

Organonickel complex *J*-aggregation on interfacial evaporator promotes broadband absorption and salt rejection for efficient solar-powered desalination

Yi-Ting Lin, Joanna S. Lin, Yung-Cong Yang, Jen-Shyang Ni [*]

Department of Chemical and Materials Engineering, Photo-sensitive Material Advanced Research and Technology Center (Photo-SMART), National Kaohsiung University of Science and Technology, Kaohsiung 80778, Taiwan

HIGHLIGHTS

- Organometallic small molecule-based interfacial evaporator for salt-resistance SSG.
- The substitution effect of thienyl and phenyl rings on molecular electron-delocalization.
- NiTh's J-aggregation on the surface triggers broadband absorption and salt resistance.
- NiTh-constructed seawater SSG has a superior evaporation rate of 2.1 kg m^{-2} h^{-1} with an exceeding 100% efficiency.

GRAPHICAL ABSTRACT

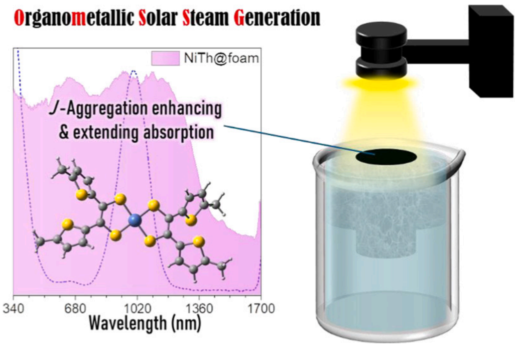

ARTICLE INFO

Keywords:
Photothermal
Solar energy
Solar steam generation
SSG

ABSTRACT

Solar steam generation (SSG) driven by environment-friendly and renewable energy is emerging as a promising technology for alleviating clean water scarcity. So far, developing solar-thermal conversion materials for solar interfacial absorbers to advance evaporation rate and efficiency is still a crucial challenge. Herein, the thienyl-substituted organonickel bis(dithiolene) complex (NiTh) with an intense second near-infrared (NIR-II) absorption of intervalence charge transfer transition was synthesized and systemically compared with the phenyl-based complex (NiPh). Based on the delocalization electron property of thiophene, NiTh behaves with low adiabatic and high reorganization energies, contributing to its nonradiative decay rate and photothermal conversion. Its *J*-aggregation on the foam fiber was fabricated as a solar-to-heating interfacial layer with broad absorption from visible to NIR-II regions and salt-resistance ability, resulting in excellent solar light-harvesting. Under one sun of irradiation, the NiTh-adsorbed foam with red-shifted absorption and higher photothermal conversion ability exhibits a faster solar energy-to-evaporation rate (1.99 ± 0.10 kg m^{-2} h^{-1}) compared with the NiPh-adsorbed foam (1.83 ± 0.06 kg m^{-2} h^{-1}), of which the blank foam is 0.48 ± 0.03 kg m^{-2} h^{-1}. The evaporation rate of solar-driven seawater desalination based on NiTh@foam evaporator can reach up to 1.80 ± 0.05 kg m^{-2} h^{-1}, and the efficiency is as high as 122.1 ± 3.1 % due to the additional energy harvesting in the side areas that absorb sunlight and the light-trapping effect inside the three-dimensional evaporator. For organic pollutant solution,

---

* Corresponding author.
E-mail address: jsni@nkust.edu.tw (J.-S. Ni).

https://doi.org/10.1016/j.desal.2024.118201
Received 24 July 2024; Received in revised form 7 October 2024; Accepted 12 October 2024

clean condensed water with an evaporation rate of 2.03–2.17 kg m^{-2} h^{-1} can be obtained through the SSG operation based on NiTh@foam. This study promotes a strategy for designing small molecules with NIR-II absorption and further modification on porous foam surfaces to achieve high-effcitive solar-driven evaporation application.

1. Introduction

With the continuous population expansion and industry development, how to obtain freshwater resources has emerged as a crucial problem and has also been one of the Sustainable Development Goals focused on by the United Nations. Conventional water purification techniques are divided into two primary methods: thermal (multi-stage flash and multi-effect distillation, and mechanical vapor compression) and membrane (reverse osmosis and electrodialysis) desalination, [1–3] removing salts and other impurities from seawater or brackish water to produce freshwater. However, these processes would suffer from drawbacks such as high energy consumption, high installation costs, and environmental impacts. By contrast, solar steam generation (SSG) technology harnesses sunlight to heat water or other fluids to produce water vapor, further condensing to freshwater for drinking or industrial water. [4] This sustainable desalination technology uses renewable and clean solar energy to drive desalination, which reduces fossil fuel reliance and carbon emissions, providing cost savings, safety, and environmental benefits over the long term. Therefore, improving the SSG system to enhance its performance has continued to be the focus of attention in desalination applications.

For the components of the SSG system, the interfacial evaporator has played an essential role in capturing and concentrating solar energy onto evaporating surfaces. [5] Herein, solar-thermal conversion materials (STCMs) were coated to surfaces within solar collectors to efficiently absorb and convert solar radiation into heat energy for steam generation. Over the past few decades, various STCMs have been developed to achieve a high solar energy-powered evaporation rate and efficiency, including carbonaceous materials, [6,7] semiconducting nanoparticles with surface plasmon resonance effect, [8–11] conjugated polymers, [12–14] organic small molecules, [15–18] etc. Among them, organic small molecules have the advantage of unambiguous chemical structures and photophysical properties, easy modifiability, trusted purity, and high product reproducibility. [19] Such characteristics are conducive to strategically improving SSG performance through molecular mechanisms [19,20] such as photoinduced nonadiabatic decay, [21] twisted intramolecular charge transfer state, [22] and intramolecular motion-induced photothermy. [23,24] Moreover, to increase the absorption range of STCMs, the general approach is to extend the conjugate length; [25,26] however, it will cause additional complex manufacturing costs. Given this issue, developing STCMs with broad absorption, high photothermal conversion, and simple preparation will be an essential priority for solar-driven desalination.

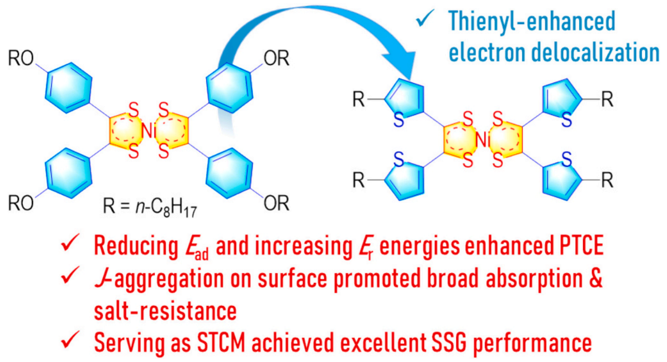

Scheme 1. The design strategy of substitution effect on organonickel bis(dithiolene) complexes.

The group 10 transition-metal bis(dithiolene) complexes are a class of coordination compounds with unique near-infrared (NIR) absorption, in which two dithiolene ligands coordinate a d^8 metal (nickel, palladium, and platinum) cation to form a square planar coordination geometry. [27,28] Compared to the traditional small molecule-type STCMs, the complexes have relatively facile preparation through a one-pot synthesis approach of nickel ion and diketonyl compound as dithiolene precursor. Therein, the dithiolene ligand can coordinate the metal center with different redox states (dithiolate, dithiolene, and dithione forms), resulting in different oxidation and mixed-valence states for the complex. [28] This nature can advance electron delocalization as well as intervalence charge transfer (IVCT) within a complex, contributing to widely intense absorption in the NIR region, [29] especially in the second NIR (NIR-II, 1000–1700 nm) window. [30,31] Additionally, based on the high reorganization energy release from molecular geometrical relaxation, the organometal bis(dithiolene) complex with a nickel center behaved with higher photothermal conversion than that with palladium and platinum centers. [30] The SSG interfacial layer based on the organonickel complex thus could achieve an excellent solar-to-vapor efficiency.

In this study, we introduced the electron-donating thienyl ring into the organonickel complex to reduce the dihedral angle of the whole molecule as well as to advance red-shifting absorption (Scheme 1). According to theoretical calculation results, the thienyl-substituent can delocalize the complex's electrons well and stabilize its highest occupied molecular orbital (HOMO) and lowest unoccupied molecular orbital (LUMO). Compared to the phenyl-substituted complex (NiPh), the organonickel complex tying thiophene (NiTh) has minor transition and adiabatic energies between the ground and excited states. This contributes to bathochromic shifting absorption and increases the non-radiative decay rate for internal conversion. [26] Upon fabricating a solar-to-heat interfacial absorber, the J-aggregation property of NiTh on the hydrophilic melamine sponge triggers broadband absorption from visible to NIR-II regions to improve solar energy utilization. The hydrophobic NiTh-modified surface also has the function of inhibiting salt accumulation and helping salt self-cleaning. As such a synergic effect, the optimized evaporation rates of NiTh-based SSG devices under one sunlight radiation are achieved at 2.16 and 2.07 kg m^{-2} h^{-1} for deionized water and seawater systems, respectively, and the solar-to-vapor efficiencies exceed 100 %. Freshwater for drinking or industrial water can also be attained further through solar-driven desalination of seawater or sewage. This investigation elucidates the molecular design concept of advancing organometallic molecules with NIR-II absorption to promote the development of highly efficient SSG performance.

2. Materials and methods

2.1. Chemicals and instrumentation

Chemicals were purchased from Acros Organics and Alfa Aesar and used directly without further purification. ^1H and ^{13}C NMR spectra were recorded on the Varian VNMRS 600 MHz spectrometer using $CDCl_3$ solvent. High-resolution mass spectra (HRMS) were recorded on an Autoflex Speed Bruker, operated in a MALDI-TOF mode. UV–vis-NIR absorption and photoluminescence (PL) spectra were recorded on a ProTrusTech spectrometer (Taiwan) with an Avantes' SensLine and MRID, respectively. The X-ray photoelectron spectrometer (XPS) was recorded on a Thermo K-Alpha. The thermogravimetric analysis (TGA)

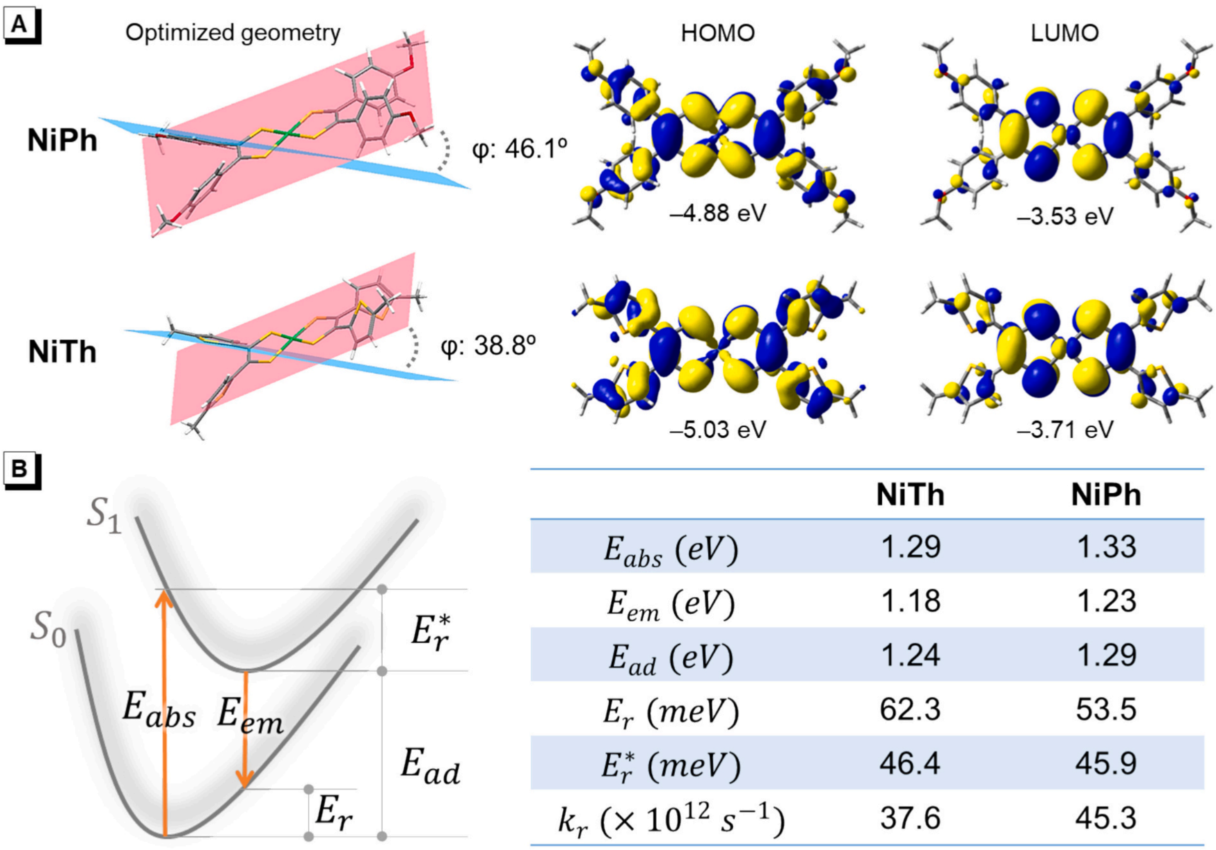

	NiTh	NiPh
E_{abs} (eV)	1.29	1.33
E_{em} (eV)	1.18	1.23
E_{ad} (eV)	1.24	1.29
E_r (meV)	62.3	53.5
E_r^* (meV)	46.4	45.9
k_r $(\times 10^{12}\ s^{-1})$	37.6	45.3

Fig. 1. Theoretical calculations of NiPh and NiTh. (A) The optimized geometries, dihedral angles (φ), and electron cloud distributions of HOMO and LUMO and their energy levels in the ground state. (B) Schematic of the ground (S_0) and excited (S_1) states and the relative transition energies. E_{abs}: absorption energy; E_{em}: emission energy; E_{ad}: adiabatic energy; E_r and E_r*: relaxation energies in S_0 and S_1 states, respectively. k_r: radiative decay rate.

was recorded on the Mettler-Toledo spectrometer, 20 °C min^{-1} of heating rate. The contact angle was measured with the OSA 60, NBSI. The scanning electron microscope (SEM) was recorded on a JSM-5610, JEOL. The inductively coupled plasma optical emission spectrometry (ICP-OES) was recorded on an iCAP 7000 Series, Thermo Scientific.

2.2. Synthesis of neutral d^8 nickel Bis-dithiolene complexes

1,2-Bis(4-(octyloxy)phenyl)ethane-1,2-dione or 1,2-bis(5-octylthiophen-2-yl)ethane-1,2-dione (2.0 equiv.) and phosphorus pentasulfide (4.7 equiv.) dissolved in 1,3-dimethyl-2-imidazo-lidinone (0.1 M) are heated at 95 °C for 10 h. A solution of $NiCl_2{\cdot}6H_2O$ (1 equiv.) in distilled water (0.4 M) is added to the mixtures and further heated at 90 °C for 2 h. After cooling, the solution is poured into distilled water and extracted with dichloromethane (CH_2Cl_2) thrice. The combined organic fractions are dried over anhydrous $MgSO_4$ and concentrated via rotary evaporation. The residue is purified by column chromatography using silica gel and CH_2Cl_2/hexanes (1/4, *v*/v) as the eluent to give a solid.

NiTh: dark-green solid, 26.9 % yield.^{1}H NMR (400 MHz, $CDCl_3$), δ (ppm): 7.11 (m, 4H), 6.70 (m, 4H), 2.77–2.73 (m, 8H), 1.70–1.65 (m, 8H), 1.29 (m, 40H), 0.91–0.87 (m, 12H). ^{13}C NMR (400 MHz, $CDCl_3$), δ (ppm): 172.78, 151.10, 140.43, 128.31, 125.28, 31.85, 31.32, 30.48, 29.29, 29.21, 29.08, 22.65, 14.10. HRMS (MALDI-TOF): calculated for $C_{52}H_7NiS_8$ $[M]^+$ 1014.3066; found: 1014.3015.

NiPh: dark-brown solid, 51.7 % yield. ^{1}H NMR (400 MHz, $CDCl_3$), δ (ppm): 7.33 (d, $J = 8.8$ Hz, 8H), 6.80 (d, $J = 9.2$ Hz, 8H), 3.96 (t, $J = 6.6$ Hz, 8H), 1.79–1.77 (m, 8H), 1.48–1.44 (m, 8H), 1.37–1.28 (m, 36H), 0.92–0.88 (m, 12H). HRMS (MALDI-TOF): calculated for $C_{60}H_{84}NiO_4S_4$ $[M]^+$ 1054.4606; found: 1054.4575.

2.3. Fabrication of SSG device

Commercially available Melamine sponges were cut into cylinders with a diameter of 18 mm and a thickness of 30 mm. NiTh with different loading amounts (1.25, 2.5, 5.0, 10.0 mg) was dissolved in dichloromethane, adsorbed on the above sponge for about 10 s (adsorption depth of 2 mm), and then dried at 40 °C for one day, preparing the solar-thermal conversion interface layer, marked as NiTh@foam. The 5.0 mg of NiPh-adsorbed sponge (NiPh@foam) and blank sponge without organonickel complex served as comparison devices. In addition, a hollow cylinder with a diameter of 45 mm and a thickness of 30 mm served as the thermal insulation and a fixture for NiTh@foam and NiPh@foam. The sponge containing organonickel complex-adsorbed foam and insulation, i.e., NiTh@foam and NiPh@foam evaporators, was placed in a 50 mL beaker filled with clean water or seawater. The evaporators are level with the water surface inside the breaker, irradiated with different solar powers (0.5, 1.0, 2.0, and 3.0 suns) for 90 min, and then simultaneously recorded water loss. For SSG cycle testing, each interval was 60 min with irradiation and then 30 min without radiation.

3. Results and discussion

3.1. Theoretical calculations of neutral nickel complexes

The theoretical calculations for ground (S_0) and excited (S_1) states of NiPh and NiTh were carried out with a time-dependent density functional theory (TD-DFT) at the level of B3LYP/6-31G(d)/LANL2DZ. For the optimized molecular geometries (Fig. 1A and S1–4), two dithiolene ligands coordinating to the typically d^8 nickel cation form the square-planar molecular configurations, which is beneficial to the

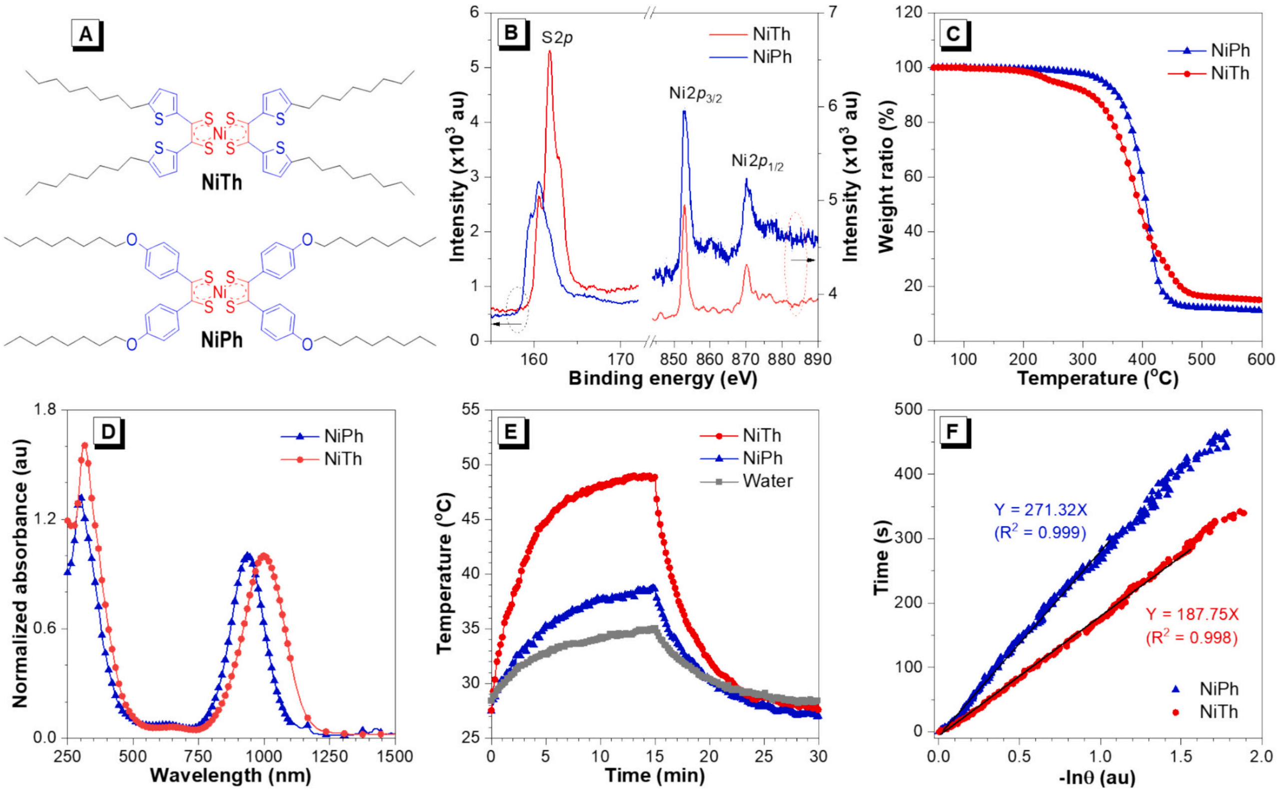

Fig. 2. Photophysical and photothermal properties of NiTh and NiPh. (A) Chemical structures, (B) XPS analysis, (C) TGA analysis, (D) normalized UV–vis-NIR absorption spectra in hexane (10 μM), (E) time-dependent temperature changes in deionized water (10 μM) under 1064 nm irradiation (1 W cm^{-1}), and (F) the plot of irradiation time versus –ln(θ) for NiPh and NiTh. θ is the driving-force temperature. The inset is the fitting equation, in which the slope indicates its system time constant (τ_s).

intermolecular stacking in the aggregation state to extend absorption in the NIR-II window. (vide infra) Compared to NiPh, the smaller dihedral angle of NiTh triggers a more electron cloud of LUMO to spread from the bis(dithiolene)nickel core into the surrounding thienyl-rings, leading to better electron-delocalization on the whole molecular skeleton. Thus, the down-shifted energy levels of HOMO and LUMO and narrower energy gap for NiTh (1.32 eV; 1.35 eV for NiPh) can be observed. Likewise, NiTh, with a smaller absorption energy (1.29 eV), exhibits a bathochromic shift wavelength than NiPh (1.33 eV) (vide infra), improving effective sunlight absorption. Further analyzing with the four-point method (Fig. 1B), [32] the reorganization energies in S_0 (E_r) and S_1 (E_r*) states are 62.3 and 46.4 meV, respectively, for NiTh, which are higher than those for NiPh. This results from more nonradiative vibrational relaxation for the former upon the configurational reorganization in the deexcitation process. Moreover, the smaller adiabatic energy (E_{ad}) between the minimum S_1 and S_0 states for NiTh (1.24 eV; 1.29 eV for NiPh) related to the higher internal conversion rate from S_1 to S_0 states leads to more nonradiative decay. On the other hand, the radiative decay rate (k_r) was estimated by the formula, [32]

$$k_r = \frac{f_{em} \times (E_{em})^2}{1.5}$$

where E_{em} and f_{em} are the first emission energy and its oscillation factor, respectively. The k_r value for NiTh is slower than that for NiPh. As such, the smaller E_{ad}, higher E_r, and slower k_r values producing more nonradiative transition for NiTh will contribute to photothermal conversion behavior and further as an STCM for the SSG system.

3.2. Optical and photothermal properties of nickel complexes

The chemical structures (Fig. 2A) and synthetic routes (Scheme S1) of neutral nickel complexes based on the bis(dithiolene) ligand and their molecular identifications are included in the Supporting Information (Fig. S5–10). For XPS analysis (Fig. 2B and S10), 853 and 870 eV of binding energies reveal the elemental compositions of the center nickel atom (Ni $2p_{3/2}$ and Ni $2p_{1/2}$) within the complexes. Compared to NiPh, NiTh has a higher S $2p$ signal, attributed to its higher sulfur content, with slightly shifted binding energy. Besides, the thermogravimetric analysis (TGA) exhibits good thermal stability of 248.7 and 332.7 °C for NiTh and NiPh, respectively, as their weight loss by 5 % (Fig. 2C). The high thermal stability of nickel complexes makes them possible applications in high-temperature SSG systems through the heterostructure fabrication process. [33,34] Regarding photophysical properties, the UV–vis-NIR absorption spectra in hexane (10 μM) present intense NIR-II absorption wavelengths of 1083.6 and 1022.2 nm for NiTh and NiPh (Fig. 2D), respectively, attributed to the delocalized ligand's IVCT transition. [35] On the other hand, the feeble ligand-to-metal charge transfer and intense π-π* transitions of nickel complexes result in visible absorption bands. Nevertheless, both with dim even no photoluminescence spectra in hexane were obtained. This suggests that the excited complexes mostly release energy through the nonradiative pathway, not radiative decay of emission, which is consistent with the theoretical calculation result. (vide supra) To understand the contribution of nonradiative decay to photothermal conversion performance, nickel complex aggregates (200 μg mL^{-1} in deionized water) were irradiated with 1064 nm of laser (1 W cm^{-2}) for 15 min, and their temperatures were up to 48.9 °C (NiTh) and 38.7 °C (NiPh), respectively (Fig. 2E). The system time constants for heat transfer (τ_s), determined by applying the linear time from the cooling period versus negative natural logarithm of the driving force temperature (Fig. 2F), are 187.8 and 271.3 s for NiTh and NiPh, respectively. Their photothermal conversion efficiencies (PTCEs) [36] are further calculated to be 48.6 % (NiTh) and 29.2 % (NiPh). This result proposes that NIR-II nickel complex-formed

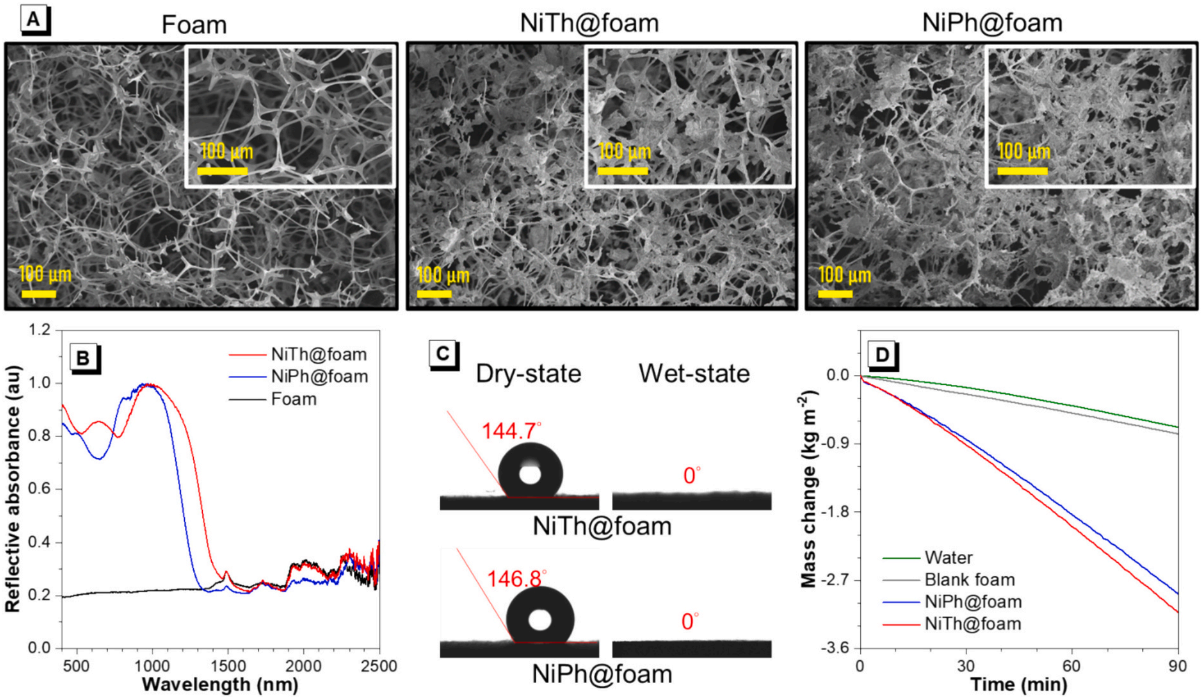

Fig. 3. The surface morphologies and solar-steam generation (SSG) of nickel complex-adsorbed foams. (A) Scanning electron microscope (SEM) images of foam, NiTh-adsorbed foam (NiTh@foam), and NiPh-adsorbed foam (NiPh@foam). (B) The reflective UV–vis-NIR absorption spectra, (C) the contact angle analysis, and (D) water-mass change curves under one sun irradiation for NiTh@foam and NiPh@foam, compared with blank foam and water only.

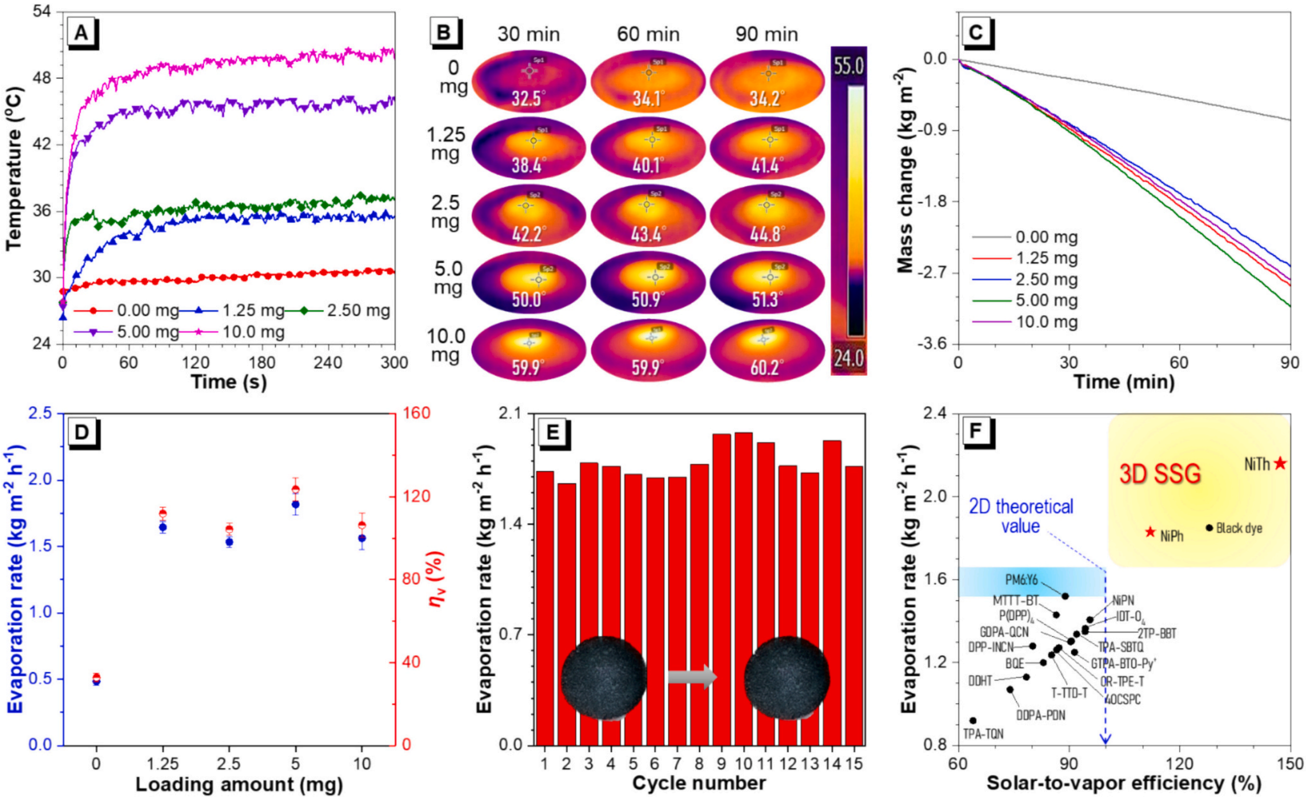

Fig. 4. SSG performance of NiTh@foam with different loading. (A) Time-dependent temperature changes, and (B) infrared images of the solar-thermal interfacial-heating evaporation layers, (C) water-mass change curves, (D) the relationship between evaporation rate (blue) and solar energy-to-vapor efficiency (η_v; red) for different amounts of NiTh-loading foams under one sun irradiation. (E) SSG stability for 5.0 mg of NiTh-loading device. The inset of (E) is the surface change of NiTh@foam before and after SSG work. (F) Small molecule-based SSG performances.

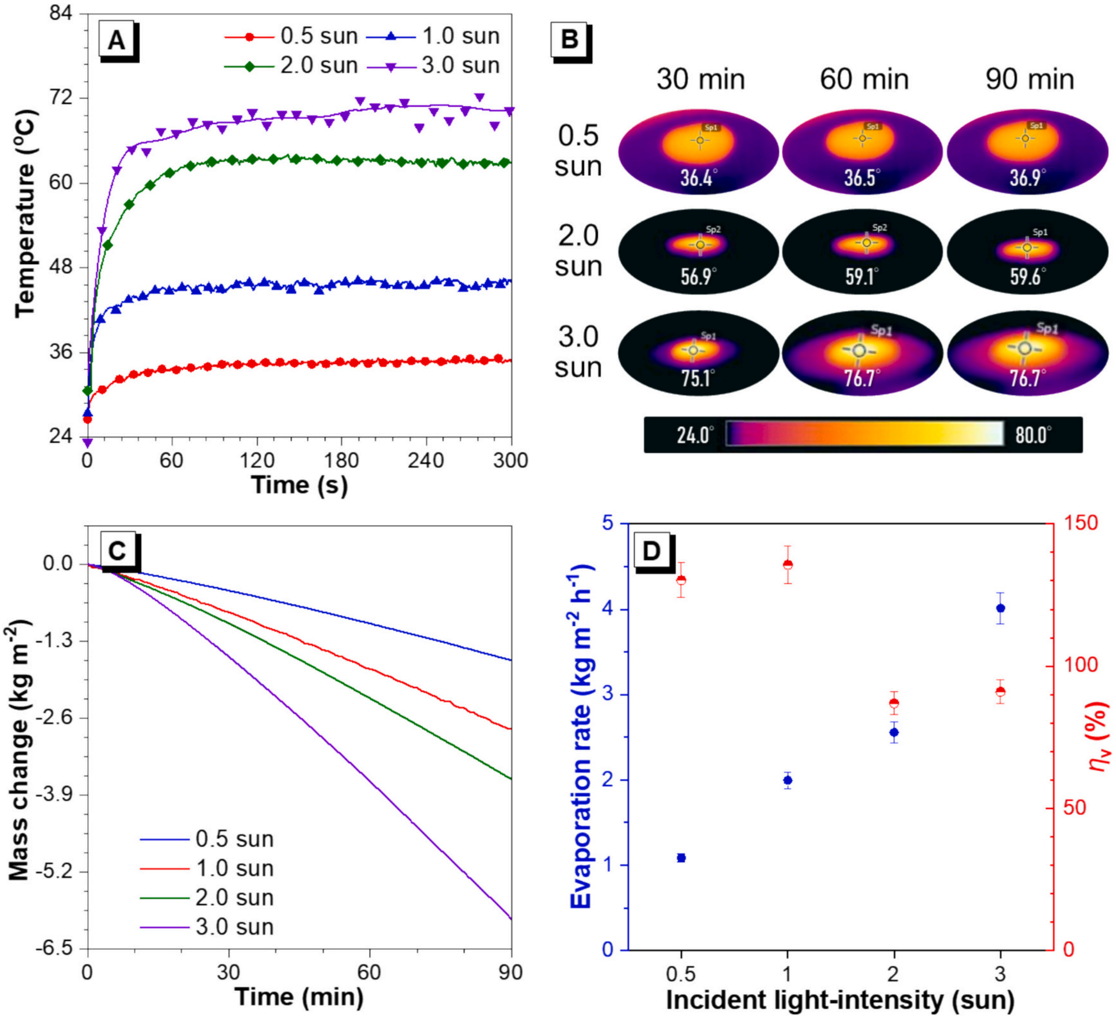

Fig. 5. SSG performance of NiTh@foam under different irradiation powers. (A) Time-dependent temperature changes, (B) infrared images of the solar-thermal interfacial-heating evaporation layers, (C) water-mass change curves, and (D) the relationship between evaporation rate (blue) and solar energy-to-vapor efficiency (η_v; red) for 5.0 mg of NiTh-loading foams under different irradiation powers.

aggregates efficiently convert light irradiation to heat energies and are suitable as a solar energy-to-vapor interfacial layer to generate freshwater. (vide infra).

3.3. Solar energy-to-vapor performances of nickel complex-based SSG devices

NiTh and NiPh, with good photothermal properties and strong absorption in the NIR region, served as the STCM and were further adsorbed on the surface of melamine foam (BASF Corporation), forming interfacial-heating evaporators for the SSG system (Fig. S11). According to the XPS analysis (Fig. S12), the unique signals of Ni are observed on the foam surface adsorbed with NiTh or NiPh, evidencing successful agglutination between nickel complexes and foam fiber. Compared to blank foam showing a smooth fiber (Fig. 3A), the rough foam surface adsorbed with NiTh (NiTh@foam) appears to have large aggregation and loose particles, whereas that with NiPh (NiPh@foam) displays evenly and intensively small-sized particles. This morphology implies that the planar NiTh efficiently gathers together on the foam. There is thus more red-shifted absorption for NiTh aggregating on the foam than that dissolved in hexane (Fig. 3B and S13), attributed to intermolecular *J*-aggregation. Compared to NiPh@foam, NiTh@foam has a broadband absorption from visible extending to 1600 nm of the NIR-II region, revealing high solar light absorbance. Moreover, the moistened nickel complex-adsorbed foams (named “wet-state”) have excellent hydrophilicity for the evaporation of water (Fig. 3C), inspiring us to fabricate solar energy-to-vapor conversion devices for SSG measurement. As shown in Fig. 3D, upon one sun (1 kW m^{-2}) irradiation over 90 min, the water-mass change through solar energy-driven evaporation was simultaneously recorded by time. The NiTh@foam evaporator shows a higher water evaporation rate ($\dot{m}$) of 1.99 ± 0.10 kg m^{-2} h^{-1} than NiPh@foam (1.83 ± 0.06 kg m^{-2} h^{-1}) one. Unlike blank foam, which has only 0.48 ± 0.3 kg m^{-2} h^{-1} of $\dot{m}$ value, nickel complexes-modified systems visibly obtain accelerated water evaporation. Subsequently, their solar energy-to-vapor efficiencies (η_v) can be calculated by the following formula: [15].

$$\eta_v = \frac{\dot{m}H}{C_{opt}P_0}$$

where C_{opt} refers to the optical concentration, P_0 is the nominal solar irradiation value of the sunlight intensity, and H denotes the total enthalpy of phase change between liquid and vapor. Interestingly, the η_v values for NiTh@foam and NiPh@foam evaporators are estimated to be 135.6 ± 6.63 % and 112.0 ± 3.95 %, respectively, over 100 % of the theoretical value. The reason may be that photothermal agents' contributions within surface pores and side areas are difficult to evaluate, especially for a three-dimensional (3D) evaporator. Like the light-trapping texture-modified evaporator [37] and porous wood-based

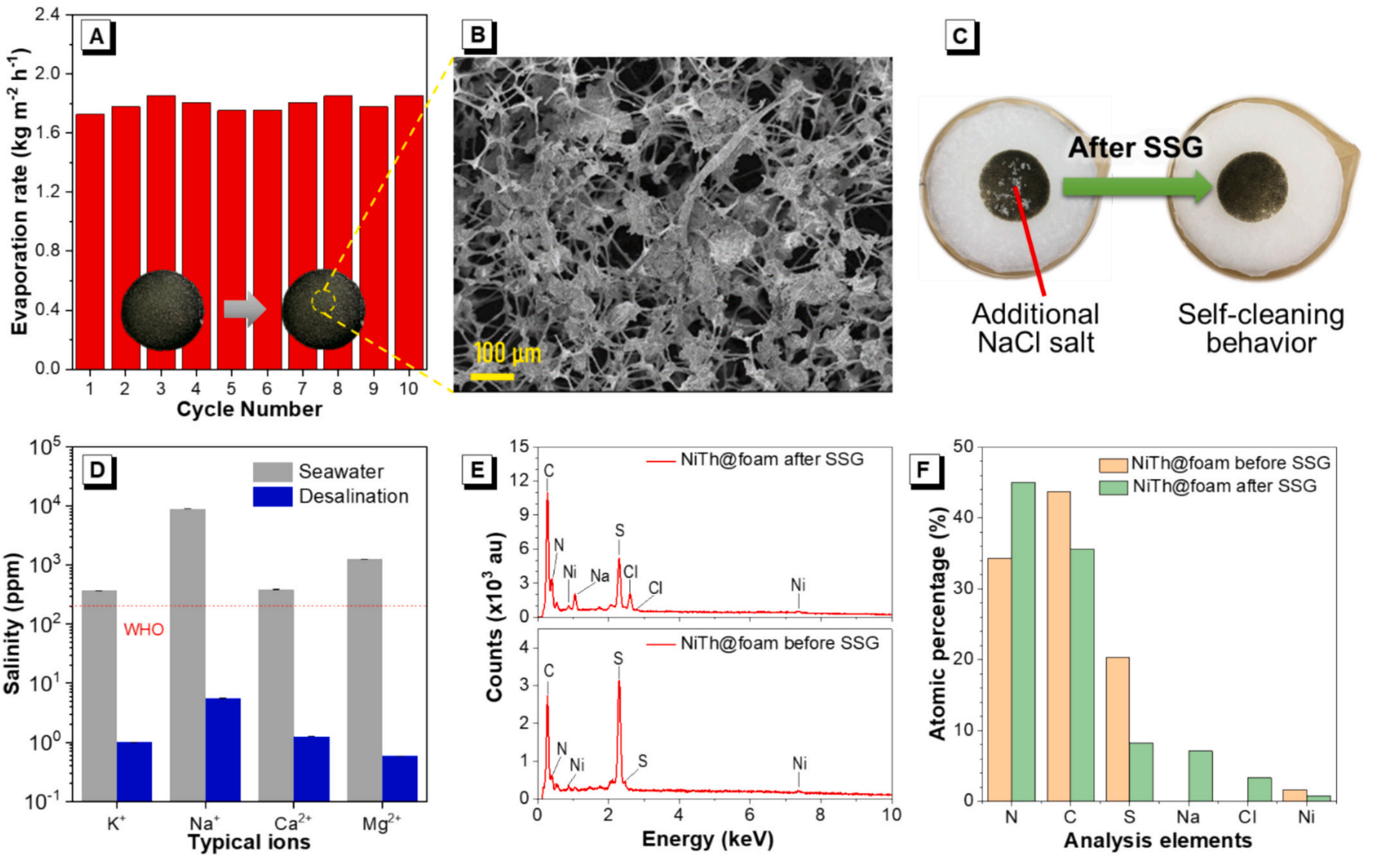

Fig. 6. Desalination application of NiTh@foam. (A) The cycle solar energy-to-evaporation of 5.0 mg of NiTh-loading SSG device for Sizihwan seawater under 1 sun irradiation. The inset pictures are the surface of NiTh@foam before and after desalination. (B) SEM images of the surface morphology of NiTh@form after desalination. (C) The self-cleaning test of NiTh@foam. (D) Four ion concentrations of the seawater before and after desalination. (E) The SEM with energy-dispersive X-ray spectroscopies for the longitudinal section of NiTh@foam before and after SSG from 26 wt% NaCl solution and (F) their elemental percentage distribution.

solar steam generator [38], NiTh@foam's porous structure (Fig. 3A) provides the capability to capture the incident solar irradiance and then reduce reflection losses and enthalpy, thereby enhancing the conversion of solar energy into heat. On the other hand, for 3D SSG evaporators, the additional energy harvesting in the side areas that absorb sunlight and the light-trapping effect inside the evaporator can contribute to solar energy-to-vapor rate, [37,39,40] resulting in the general calculations of $\dot{m}$ value will be higher than the theoretical values for 2D evaporators (1.5–1.6 kg m^{-2} h^{-1}). [41] The same phenomenon of over 100 % efficiency has also been reported. [42–45] Despite the efficiency above the theoretical value, the tendency for NiTh@foam to have better solar energy-driven evaporation than NiPh@foam is quite reliable. As a consequence, the SSG system based on the NiTh@foam evaporator will be systematically studied.

3.4. *Solar energy-to-vapor performances of NiTh@foam evaporator*

To assess the impact of NiTh-loading on the interfacial-heating layer, NiTh@foam evaporators with different adsorption quantities (1.25, 2.50, 5.00, and 10.0 mg) were fabricated for SSG measurement. With increasing NiTh amounts on the foam, the absorptions from visible to NIR regions for foam surface approach saturation. This thus results in the equilibrium temperatures of the interfacial evaporation layer rise in the order of 34.5 °C (1.25 mg), 37.4 °C (2.5 mg), 44.4 °C (5.0 mg), and 51.2 °C (10.0 mg) under solar irradiation (1 sun, 1 kW m^{-2}) for 5 min (Fig. 4A). After 90 min irradiation, their temperatures reach 41.4 (1.25 mg), 44.8 (2.5 mg), 51.3 (5.0 mg), and 60.2 °C (10.0 mg), respectively, whereas that only 34.2 °C without nickel complex-loading (Fig. 4B). Gathering time-dependent water-mass change as shown in Fig. 4C and D, the 5.0 mg NiTh-loading evaporator delivers the best evaporation rate of 1.99 ± 0.10 kg m^{-2} h^{-1} and efficiency under 1-sun irradiation in comparison with the others, 1.85 ± 0.07, 1.69 ± 0.06, and 1.78 ± 0.05 kg m^{-2} h^{-1} for 1.25, 2.5 mg, and 10.0 mg, respectively. According to SEM images of NiTh@foam surfaces (Fig. S14–16), with increasing NiTh metering over 2.5 mg, the pore size gradually shrinks due to the formation of large aggregations on coarse fiber, leading to blocked water transport channels that reduce water evaporation rates, especially the 10.0 mg NiTh-loading surface (Fig. S16). This means adjusting the optimal quantity of STCM within the foam favors the interfacial heating effect. Moreover, the reusability and stability of the SSG system based on the 5.0 mg-NiTh@foam evaporator were confirmed by using 15 cycles of evaporated experiments, in which 1.5 h of radiation for each cycle (Fig. 4E). The foam's surface almost no change before and after work (The inset of Fig. 4E). After optimization, the best water evaporation rate can be achieved at 2.160 kg m^{-2} h^{-1} with 147.2 % of efficiency. Compared with small molecule-adsorbed solar evaporators (Fig. 4F), the 3D SSG devices with side area's light-harvesting and pore's light-trapping effects behave more excellent in performance. According to reports, the highest water evaporation rate can even reach up to 10.07 kg m^{-2} h^{-1}, with an efficiency of 239.66 %. [40] This signifies that the 3D-constructed NiTh@foam photoabsorber has certain advantages in efficiently and stably converting solar energy into heat and exhibiting excellent SSG performance.

Inspecting the effect of incident-light intensity, SSG devices with 5.0 mg NiTh-loading were irradiated under different power intensities (0.5, 2.0, and 3.0 sun). As light intensity is enhanced to 3 suns, the equilibrium temperature rises to 76.7 °C (Fig. 5A and B), and the water evaporation rate reaches as high as 4.01 ± 0.18 kg m^{-2} h^{-1} (Fig. 5C), higher

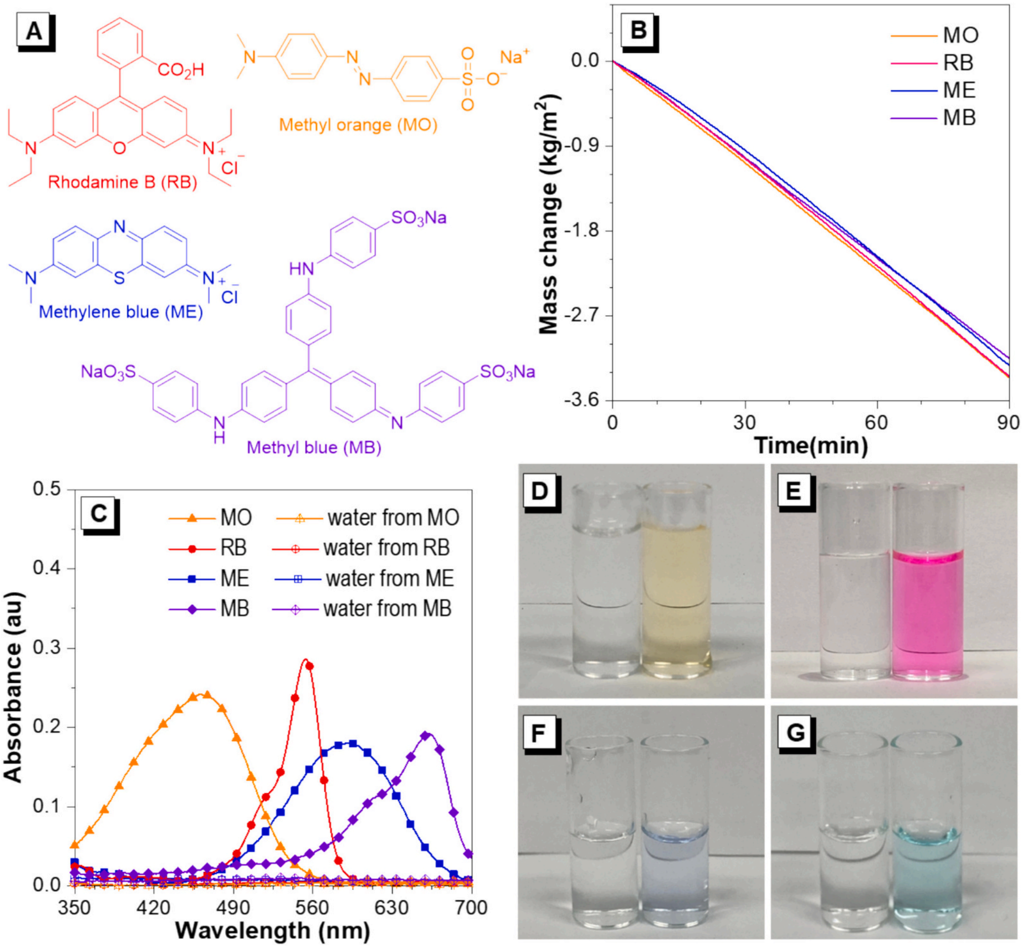

Fig. 7. Solar-driven evaporation from organic pollution water. (A) The chemical structures, (B) time-dependent water-mass change curves under one sun irradiation, and (C) UV–vis absorption spectra of typical organic pollutants (MO: methyl orange; RB: rhodamine B; ME: methylene blue; MB: methyl blue) and their condensed water. (D–G) Photographs of MO (D), RB (E), ME (F), and MB (G) solution and corresponding condensed water.

than the other irradiations, 1.09 ± 0.05 and 2.56 ± 0.12 kg m^{-2} h^{-1} for 0.5 and 2.0 suns, respectively. The $\dot{m}$ values increase with increasing light intensity. After estimating by dividing with power density, the solar energy-to-vapor efficiencies are 130.2 ± 6.1 % for 0.5-sun, 86.9 ± 4.1 % for 2.0-sun, and 90.9 ± 4.1 % for 3.0-sun (Fig. 5D). On the whole, the NiTh-adsorbed foam as an interfacial solar vapor generator under irradiation of one sunlight behaves the best SSC performance.

3.5. Solar-driven desalination for NiTh@foam evaporator

Solar-driven steam generation experiments based on the NiTh@foam evaporator were carried out with Sizihwan seawater (Kaohsiung, Taiwan) to demonstrate the seawater purification ability of a NiTh-constructed device. As shown in Fig. 6A, the NiTh@foam exhibits a stable evaporation rate of 1.80 ± 0.05 kg m^{-2} h^{-1} under one sun for at least 10 cycles. The surface morphologies of NiTh@foam are almost unchanged, and there is no salt accumulation after and before SSG cycle tests, whether under microscopic or macroscopic observation (Fig. 6B and the inset of Fig. 6A). The average efficiency is estimated at 122.1 ± 3.1 %, declining 13.5 % compared to the deionized water sample. In general, this results from the decreasing vapor pressure of the former. To further explore the salt removal ability of the NiTh@foam, an additional NaCl was placed on the NiTh@foam's surface for evaporation experiments. As shown in Fig. 6C, NaCl dissolves within 300 s, signifying that the NiTh@foam can avoid sea salts accumulating on the evaporator's surface, contributing to a smooth solar-driven desalination process. The self-cleaning ability against salt comes from the hydrophobic NiTh-modified foam surface, avoiding salt precipitation on one. [46] Herein, the typical four metal ions of seawater and evaporation water were measured by an ICP-OES (Fig. 6D). Compared to seawater, the cations' contents of evaporation water are dropping by three orders of magnitude, which aligns with the World Health Organization's drinking water standards. In addition, to express the self-cleaning capability of the NiTh@foam evaporator, its SSG performance from high salinity solution (26 wt% NaCl) was further measured. As shown in Fig. S18, the solar-driven desalination evaporation rates are 1.55–1.62 kg m^{-2} h^{-1}, the average efficiency is 106.7 ± 2.5 %, and the surface IVCT absorption is similar before and after operation (Fig. S19).

To gain insight into the self-cleaning and capillary behaviors of the NiTh@foam evaporator, the longitudinal section of foam and NiTh@foam before and after SSG in 26 wt% NaCl solution were measured by scanning electron microscopy with energy-dispersive X-ray spectroscopy (SEM-EDX), and the results were collected in Figs. 6E and F and S20–24. After operating in a high-salinity solution, some NaCl crystals can be observed in the longitudinal section of NiTh@foam (Fig. S22A), where Na and Cl elements accounted for 7.12 % and 3.33 % of the total analyzed elements, respectively (Fig. 7F). In comparison, 13.19 % of Na and 14.98 % of Cl atoms are also found on the foam fibers (Fig. S24). The slight decrease in SSG efficiency results from the reduced vapor pressure and slight salt deposition in high-salinity solution. However, while the salt is transported upward to the surrounding foam and NiTh@foam via the steam-driven capillary effect, the effect can also redissolve the salt back into the solution to avoid salt deposition and enable self-cleaning behavior. On the other hand, the self-cleaning ability of the

NiTh@foam evaporator exhibits only slight salt accumulation on the foam fiber even when operating in a high-salinity solution (Fig. S18). As such, the NiTh@foam evaporator performs well and is stable for high-salinity water and general seawater (salt concentration around 3.5 %). Thereafter, four organic dye (MO, RB, ME, and MB) solutions were selected as simulated sewage to test the purification capacity through the NiTh@foam-based SSG system (Fig. 7). According to UV–vis absorption spectra (Fig. 7C), the disappearance of the dye's characteristic absorption peaks for the condensed water proves that the freshwater is free from any residues. The condensed water with evaporation rates of 2.03–2.17 $\mathrm{kg\,m^{-2}\,h^{-1}}$ (Fig. 7B) from pollution solutions is transparent to the naked eye in daylight (the left of Fig. 7D-G). All in all, the NiTh-adsorbed evaporator realizes freshwater acquisition through solar energy-driven desalination or sewage evaporation. Finally, taking the fabrication cost into consideration, the estimated cost of a large-area NiTh@foam evaporator is approximately $793 per square meter (Table S1). Although the development cost of NiTh is lower than that of organic photothermal conversion materials, [47,48] it is a challenge compared with reported inorganic or carbide-based SSG systems. [49,50] In addition to improving the synthesis process to reduce costs, increasing the multifunctional properties of NiTh-based evaporators, such as photodynamic, thermoelectric, and anti-adhesion behaviors, to enhance their cost-effectiveness will make them viable prospects for practical applications.

4. Conclusion

This study successfully synthesized the thienyl-tied organonickel complex (NiTh) and systemically likened it with the phenyl-based one (NiPh) to explore the substitution effect on the dithiolene ligand. Thanks to better delocalization electron properties of thiophene-donor, NiTh has lower transition and adiabatic and higher reorganization energies than NiPh, leading to more nonradiative energy release for improving photothermal conversion performance. Upon NiTh adsorbed on the porous sponge, its *J*-aggregation on the surface induces broad UV–vis-NIR absorption and hydrophobic interfacial modification, improving solar-light utilization and salt-rejection ability, respectively. The NiTh-based solar-thermal heating interfacial absorber thus can realize as high as 1.99 ± 0.10 and 1.80 ± 0.05 $\mathrm{kg\,m^{-2}\,h^{-1}}$ of evaporation rates for deionized water and seawater, respectively, with efficiencies exceeding 100 % under one sun of irradiation. Through the NiTh-based SSG system, the typical seawater cations and sewage's organic pollutants can be removed to acquire freshwater for drinking and industrial water. This investigation demonstrates the potential of small molecule-type organometallic complexes to be applied to SSG technology through structural modifiability, and it also provides a strategical approach to design STCMs for sustainable solar-driven desalination and wastewater treatment.

Author contribution

The manuscript was written with contributions from all authors. All authors have approved the final version of the manuscript.

Declaration of competing interest

The authors declare the following financial interests/personal relationships which may be considered as potential competing interests:

Jen-Shyang Ni reports financial support was provided by National Science and Technology Council (TW). If there are other authors, they declare that they have no known competing financial interests or personal relationships that could have appeared to influence the work reported in this paper.

Acknowledgments

We are grateful for financial support from the National Science and Technology Council (NSTC 111-2113-M-992-001-MY2 and NSTC 113-2113-M-992-001, Taiwan) and theoretical calculation support from the National Center for High-Performance Computing (NCHC, Taiwan).

Appendix A. Supplementary data

Supplementary data to this article can be found online at https://doi.org/10.1016/j.desal.2024.118201.

Data availability

The data that has been used is confidential.

References

[1] N.M.A. Omar, M.H.D. Othman, Z.S. Tai, M.F. Rabuni, A.O.A. Amhamed, M. H. Puteh, J. Jaafar, M.A. Rahman, T.A. Kurniawan, Overcoming challenges in water purification by nanocomposite ceramic membranes: a review of limitations and technical solutions, J. Water Process Eng. 57 (2024) 104613.

[2] L. Huang, L. Ding, J. Caro, H. Wang, Mxene-based membranes for drinking water production, Angew. Chem. Int. Ed. 62 (2023) e202311138.

[3] T.M. Joseph, H.E. Al-Hazmi, B. Sniatala, A. Esmaeili, S. Habibzadeh, Nanoparticles and nanofiltration for wastewater treatment: from polluted to fresh water, Environ. Res. 238 (2023) 117114.

[4] W. Shang, T. Deng, Solar steam generation: steam by thermal concentration, Nat. Energy 1 (2016) 16133.

[5] Y. Liu, J. Zhao, S. Zhang, D. Li, X. Zhang, Q. Zhao, B. Xing, Advances and challenges of broadband solar absorbers for efficient solar steam generation, Environ. Sci. Nano 9 (2022) 2264–2296.

[6] M. Toyoda, M. Inagaki, Carbon materials for solar steam-generation, Carbon 214 (2023) 118373.

[7] M.N.A.S. Ivan, S. Saha, A.M. Saleque, S. Ahmed, A.K. Thakur, G. Bai, Z. Miao, R. Saidur, Y.H. Tsang, Progress in interfacial solar steam generation using low-dimensional and biomass-derived materials, Nano Energy 120 (2024) 109176.

[8] L. Noureen, Q. Wang, P.M. Ismail, M. Alomar, N. Arshad, M.S. Irshad, Q. Xu, X. Wang, Multifunctional aerogel with antibiofouling properties for efficient solar steam generation and seawater desalination, Nano Today 54 (2024) 102130.

[9] J. Wu, D. Liu, Y. Sun, B. Wei, K. Dai, Y. Sun, F. Zhang, C. Li, J. Xue, Z. Zhu, X. Gao, Q. Zheng, Ultralight anisotropic $Ti_3C_2T_X$ mxene/carbon nanotube hybrid aerogel for highly efficient solar steam generation, Carbon 223 (2024) 118976.

[10] Z. Yang, Y. Wu, C. Han, Y. Quan, Y. Li, W. Wang, X. Min, J. Xiong, M. Li, Fe_3O_4-polyvinyl alcohol sponge as photo-absorber in interfacial solar steam generation, Desalination 564 (2023) 116796.

[11] Y. Zhang, Y. Wang, B. Yu, K. Yin, Z. Zhang, Hierarchically structured black gold film with ultrahigh porosity for solar steam generation, Adv. Mater. 34 (2022) e2200108.

[12] C.Y. Lin, T. Michinobu, Conjugated photothermal materials and structure design for solar steam generation, Beilstein J. Nanotechnol. 14 (2023) 454–466.

[13] R. Fu, X. Cao, H. Zhang, L. Yang, Z. Zhu, W. Liang, J. Li, H. Sun, A. Li, High-efficient solar steam generation assisted removal of radioactive iodine ions from water by carbonized conjugated microporous polymer-based photothermal conversion materials, Sep. Purif. Technol. 330 (2024) 125283.

[14] M. Wang, C.Y. Lin, Y. Sagara, T. Michinobu, Enhanced photothermal property of NDI-based conjugated polymers by copolymerization with a thiadiazolobenzotriazole unit, ACS Mater. Au 4 (2024) 82–91.

[15] G. Chen, J. Sun, Q. Peng, Q. Sun, G. Wang, Y. Cai, X. Gu, Z. Shuai, B.Z. Tang, Biradical-featured stable organic-small-molecule photothermal materials for highly efficient solar-driven water evaporation, Adv. Mater. 32 (2020) e1908537.

[16] J. Dai, S. Qi, M. Zhao, J. Liu, T. Jia, G. Liu, F. Liu, P. Sun, B. Li, C. Wang, J. Zhou, G. Lu, Donor-acceptor molecule with TICT character: a new design strategy for organic photothermal material in solar energy, Chem. Eng. J. 471 (2023) 144745.

[17] R. Zhang, N. Jin, T. Jia, L. Wang, J. Liu, M. Nan, S. Qi, S. Liu, Y. Pan, A narrow-bandgap photothermal material based on a donor-acceptor structure for the solar-thermal conversion application, J. Mater. Chem. A 11 (2023) 15380–15388.

[18] L. Guo, X. Kong, R. Li, J. Sun, G. Wang, X. Gu, Low-molecular-weight organic small-molecule photothermal material for high-efficiency solar-thermal water evaporation, Dyes Pigments 227 (2024) 112195.

[19] G. Wang, B.Z. Tang, X. Gu, Manipulation of nonradiative process based on the aggregation microenvironment to customize excited-state energy conversion, Acc. Chem. Res. 57 (2024) 1360–1371.

[20] J. Huang, Z. Wang, W. Zhu, Y. Li, Solution-processed D-A-π-A-D radicals for highly efficient photothermal conversion, Aggregate 5 (2024) e426.

[21] J.-S. Ni, X. Zhang, G. Yang, T. Kang, X. Lin, M. Zha, Y. Li, L. Wang, K. Li, A photoinduced nonadiabatic decay-guided molecular motor triggers effective photothermal conversion for cancer therapy, Angew. Chem. Int. Ed. 59 (2020) 11298–11302.

[22] M. Zha, X. Lin, J.S. Ni, Y. Li, Y. Zhang, X. Zhang, L. Wang, K. Li, An ester-substituted semiconducting polymer with efficient nonradiative decay enhances

NIR-II photoacoustic performance for monitoring of tumor growth, Angew. Chem. Int. Ed. 59 (2020) 23268–23276.

[23] X. Duan, Q. Zhang, Y. Jiang, X. Wu, X. Yue, Y. Geng, J. Shen, D. Ding, Semiconducting polymer nanoparticles with intramolecular motion-induced photothermy for tumor phototheranostics and tooth root canal therapy, Adv. Mater. 34 (2022) e2200179.

[24] Z. Zhao, C. Chen, W. Wu, F. Wang, L. Du, X. Zhang, Y. Xiong, X. He, Y. Cai, R.T. K. Kwok, J.W.Y. Lam, X. Gao, P. Sun, D.L. Phillips, D. Ding, B.Z. Tang, Highly efficient photothermal nanoagent achieved by harvesting energy via excited-state intramolecular motion within nanoparticles, Nat. Commun. 10 (2019) 768.

[25] D. Li, W. He, X. Lin, X. Cui, S. Nagl, A.R. Wu, R.T.K. Kwok, R. Wu, B.Z. Tang, Enzyme-free photothermally amplified fluorescent immunosorbent assay (PAFISA) for sensitive cytokine quantification, Aggregate 4 (2023) e384.

[26] H. Li, Q. Li, Y. Gu, M. Wang, P. Tan, H. Wang, L. Han, Y. Zhu, F. He, L. Tian, Dimerization extends π-conjugation of electron donor-acceptor structures leading to phototheranostic properties beyond the sum of two monomers, Aggregate 5 (2024) e528.

[27] B. Ding, M.B. Solomon, C.F. Leong, D.M. D'Alessandro, Redox-active ligands: recent advances towards their incorporation into coordination polymers and metal-organic frameworks, Coord. Chem. Rev. 439 (2021) 213891.

[28] B. Garreau-de Bonneval, K.I. Moineau-Chane Ching, F. Alary, T.-T. Bui, L. Valade, Neutral d^8 metal bis-dithiolene complexes: synthesis, electronic properties and applications, Coord. Chem. Rev. 254 (2010) 1457–1467.

[29] M.D. Roy, T.P. Gompa, S.M. Greer, N. Jiang, L.S. Nassar, A. Steiner, J. Bacsa, B. W. Stein, H.S. La Pierre, Intervalence charge transfer in nonbonding, mixed-valence, homobimetallic ytterbium complexes, J. Am. Chem. Soc. 146 (2024) 5560–5568.

[30] Y.-C. Yang, J.S. Lin, J.-S. Ni, Neutral d^8 metal complexes with intervalence charge-transfer transition trigger an effective NIR-ii photothermal conversion for solar-driven desalination, J. Mater. Chem. A 11 (2023) 26164–26172.

[31] J.B. Pluta, R. Guechaichia, A. Vacher, N. Bellec, S. Cammas-Marion, F. Camerel, Investigations of the photothermal properties of a series of molecular gold-bis (dithiolene) complexes absorbing in the NIR-III region, Chem. Eur. J. 29 (2023) e202301789.

[32] J.-S. Ni, G.-H. Lu, Natural protoberberine alkaloid-montmorillonite nanocomposite powders with AIE features for visualizing high-resolution latent fingerprints, Spectrochim. Acta A Mol. Biomol. Spectrosc. 300 (2023) 122908.

[33] X. Wang, Y. Liu, R. Feng, Y. Zhang, C. Chang, B. Fu, T. Luan, P. Tao, W. Shang, J. Wu, C. Song, T. Deng, Solar-driven high-temperature steam generation at ambient pressure, Prog. Nat. Sci. Mater. Int. 29 (2019) 10–15.

[34] A.M. Saleque, S. Ahmed, M.N.A.S. Ivan, M.I. Hossain, W. Qarony, P.K. Cheng, J. Qiao, Z.L. Guo, L. Zeng, Y.H. Tsang, High-temperature solar steam generation by MWCNT-$HfTe_2$ van der Waals heterostructure for low-cost sterilization, Nano Energy 94 (2022) 106916.

[35] C.M. Amb, C.L. Heth, S.J. Evenson, K.I. Pokhodnya, S.C. Rasmussen, Thiophene-fused nickel dithiolenes: a synthetic scaffold for highly delocalized π-electron systems, Inorg. Chem. 55 (2016) 10978–10989.

[36] J.-B. Pluta, N. Bellec, F. Camerel, Investigation of the photothermal properties of a large series of metal-bis(dithiolene) complexes: impact of the molecular structure and ranking using the photothermal index I_{pt}, Dyes Pigments 226 (2024) 112130.

[37] A.M. Saleque, M.N.A.S. Ivan, S. Ahmed, Y.H. Tsang, Light-trapping texture bio-hydrogel with anti-biofouling and antibacterial properties for efficient solar desalination, Chem. Eng. J. 458 (2023) 141430.

[38] Q.F. Guan, Z.M. Han, Z.C. Ling, H.B. Yang, S.H. Yu, Sustainable wood-based hierarchical solar steam generator: a biomimetic design with reduced vaporization enthalpy of water, Nano Lett. 20 (2020) 5699–5704.

[39] H. Li, W. Zhu, M. Li, Y. Li, R.T.K. Kwok, J.W.Y. Lam, L. Wang, D. Wang, B.Z. Tang, Side area-assisted 3D evaporator with antibiofouling function for ultra-efficient solar steam generation, Adv. Mater. 33 (2021) e2102258.

[40] C. Shao, B. Guo, B. Lu, J. Yu, H. Kong, B. Wang, M. Ding, C. Li, PDI-based organic small molecule regulated by inter/intramolecular interactions for efficient solar vapor generation, Small 19 (2023) e2305856.

[41] Y. Shi, R. Li, Y. Jin, S. Zhuo, L. Shi, J. Chang, S. Hong, K.-C. Ng, P. Wang, A 3D photothermal structure toward improved energy efficiency in solar steam generation, Joule 2 (2018) 1171–1186.

[42] H.W. Lim, S.H. Park, S.J. Lee, 3D thermoresponsive hydrogel with enhanced water uptake and active evaporation for effective interfacial solar steam generation, Desalination 550 (2023) 116368.

[43] Z. Zhang, Z. Feng, H. Qi, Y. Chen, Y. Chen, Q. Deng, S. Wang, Carbonized sorghum straw derived 3D cup-shaped evaporator with enhanced evaporation rate and energy efficiency, Sustain. Mater. Technol. 32 (2022) e00414.

[44] X. Zhang, L. Ren, J. Xu, B. Shang, X. Liu, W. Xu, Magnetically driven tunable 3D structured Fe_3O_4 vertical array for high-performance solar steam generation, Small 18 (2022) e2105198.

[45] B. Jin, T. Cui, Y. He, M. Zhang, Y. Qi, C. Ye, 3D cellulose-based solar evaporator with tunable porous structures for high steam generation, Adv. Sustain. Syst. 8 (2024) 2300670.

[46] S.P. Prakoso, S.S. Sun, R. Saleh, Y.T. Tao, C.L. Wang, Tailoring photophysical properties of diketopyrrolopyrrole small molecules with electron-withdrawing moieties for efficient solar steam generation, ACS Appl. Mater. Interfaces 13 (2021) 38365–38374.

[47] J.C. Yang, L. Wu, L. Wang, R. Ren, P. Chen, C. Qi, H.T. Feng, B.Z. Tang, An efficient photothermal conversion material based on D-A type luminophore for solar-driven desalination, Aggregate 5 (2024) e535.

[48] S.Q. Li, Y. Deng, J. Huang, P. Wang, G. Liu, H.L. Xie, Light-absorbing copolymers of polyimides as efficient photothermal materials for solar water evaporation, Aggregate 4 (2023) e371.

[49] S. Ma, Q. Wang, K. Chen, W. Yuan, X. Gao, N. Li, N. Gao, Biomass waste-derived solar evaporator for efficient and low-cost water evaporation, Energ. Technol. 10 (2022) 2200900.

[50] W. Ruan, H. Zhang, J. Fu, Z. Li, J. Huang, Z. Liu, S. Zeng, Z. Chen, X. Li, Z. Yu, X. Liang, J. Ma, Dissolution manufacturing strategy for designing efficient and low cost polymeric solar water evaporator, Adv. Funct. Mater. 34 (2024) 2312314.

Jen-Shyang Ni received his MS degree from National Central University in 2006 under the supervision of Prof. Ming-Chou Chen, and his Ph.D. degree from National Taiwan University in 2013 under the supervision of Prof. King-Fu Lin. In 2013–2018, he carried out his postdoctoral work on novel free-metal sensitizers for dye-sensitized solar cells in the Jiann T. Lin group and aggregation-induced emission (AIE) materials for biological applications in the Ben Zhong Tang group, respectively. From 2018 to 2020, he was a research associate professor at the Southern University of Science and Technology. He is now an assistant professor in the Department of Chemical and Materials Engineering at NKUST. His research interest is creating new functional conjugation materials with novel structures and unique properties for photoelectric devices and biological theranostics applications. He mainly explains the design strategy for high-performance materials through theoretical calculation and photophysical identification. His research involves organic and organometallic chemistry, polymer, material science, computational simulation, and biomedicine. He published over 70 SCI journals, cited over 2300 times (*H*-index: 25).